



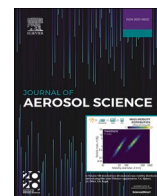
Engineered Pd-Ga alloy nanoparticles through spark ablation and in-flight metal-organic precursor decomposition

Downloaded from: <https://research.chalmers.se>, 2025-12-07 08:00 UTC


Citation for the original published paper (version of record):

Bermeo, M., Snellman, M., Jönsson, L. et al (2026). Engineered Pd-Ga alloy nanoparticles through spark ablation and in-flight metal-organic precursor decomposition. *Journal of Aerosol Science*, 191.
<http://dx.doi.org/10.1016/j.jaerosci.2025.106698>

N.B. When citing this work, cite the original published paper.



Engineered Pd-Ga alloy nanoparticles through spark ablation and in-flight metal-organic precursor decomposition

Marie Bermeo^{a,*} , Markus Snellman^a, Linnéa Jönsson^a, Thomas Krinke^a, Zhongshan Li^b, Knut Deppert^a, Maria E. Messing^{a,c}

^a Division of Solid State Physics and NanoLund, Lund University, P.O. Box 118, 22100, Lund, Sweden

^b Division of Combustion Physics, Lund University, P.O. Box 118, 22100, Lund, Sweden

^c Department of Microtechnology and Nanoscience, Chalmers University of Technology, 412 96, Gothenburg, Sweden

ARTICLE INFO

Keywords:

Nanoparticles
Spark ablation
Pd-Ga
Metal-organic
TMGa

ABSTRACT

Pd-Ga alloy nanoparticles with tunable compositions were produced by combining spark ablation with a downstream injection of a metal-organic precursor. This dual-process approach enables control over nanoparticle composition and morphology by adjusting precursor flow rate and sintering temperature. At lower precursor flows, uniform Pd-Ga nanoparticles form, exhibiting stable Pd₅Ga₂ and Pd₂Ga phases. HRTEM and STEM-EDX analyses reveal that as precursor supply increases, Ga incorporation intensifies, leading to structural transitions, phase segregation, and the formation of PdGa dominated phases with amorphous Ga-rich domains, influencing nanoparticle shape and crystallinity. This process unlocks pathways for tailoring alloy compositions in-flight with low-melting point materials.

1. Introduction

Spark ablation has emerged as a promising technique for generating nanoparticles due to its versatility in producing high-purity nanoparticles with precise control over their size, composition, and concentration. Spark ablation operates by generating high-frequency electrical sparks between two electrodes of the desired materials (Meuller et al., 2012). The energy from the sparks ablates material from the electrode surface, creating a vapour cloud that nucleates, coalesces, and condenses into nanoparticles, which are transported in a gas flow as an aerosol for further processing and deposition. The process allows for the generation of nanoparticles with complex compositions, including alloys (Ternero et al., 2024), oxides (Efimov et al., 2016), and core-shell structures (Snellman et al., 2021), by utilizing electrodes composed of multiple elements or by introducing reactive gases during the particle generation stage (Elmroth Nordlander et al., 2023; Hallberg et al., 2018). For example, previous studies have reported the generation of bimetallic nanoparticles, such as Ag-Au (Jönsson et al., 2024), Cu-Ni (Muntean et al., 2016), and Pd-Cu (Franzén et al., 2023), with tunable compositions by employing mixed-element electrodes. These alloy nanoparticles exhibit enhanced material properties compared to their single-element constituents, depending on the combination of elements and their proportions. The excellent mixing capabilities make spark ablation an attractive technique for producing nanomaterials with customized functionalities.

Despite the many advantages of spark ablation, there are significant challenges when it comes to generating alloy nanoparticles with low-melting-point materials. In spark ablation, the electrodes must be solid to generate sparks and ablate material. However,

* Corresponding author.

E-mail address: marie.bermeo_vargas@ftf.lth.se (M. Bermeo).

materials with low melting points, such as gallium (Ga), indium (In), and caesium (Cs), among others, are difficult to use as electrodes because they can melt or deform under the high-energy conditions of the spark process. This limits the ability to generate alloy nanoparticles containing such elements directly via spark ablation. To overcome this limitation, we propose an alternative approach, consisting of introducing a precursor material into the aerosol stream. For instance, a metal-organic precursor, which contains the desired low-melting-point metal, can be injected into the gas flow, where it decomposes to release metal atoms. These atoms can then alloy with the nanoparticles formed by the spark ablation process. This method allows the incorporation of elements that would otherwise be difficult to introduce using solid electrodes.

The nanoparticle generation via aerosol techniques, using low-melting point metals was previously studied by Deppert et al. (1998). Their method involved producing aerosol metal nanoparticles (Ga or In) via evaporation/condensation, mixed with a downstream injection of a hydride (ammonia, phosphine, or arsine), which was thermally cracked at elevated temperatures. This process ultimately resulted in the formation of III-V semiconductor nanocrystals.

In this study, an attractive candidate to explore is the production of Pd-Ga alloys. Pd-Ga nanoparticles have shown good performance in various catalytic processes. Pd is well-known for its catalytic activity, especially in reactions such as hydrogenation and dehydrogenation, where it facilitates the addition or removal of hydrogen atoms from organic molecules (Gryaznov et al., 1983). By alloying Pd with Ga, the catalytic properties can be significantly enhanced. Ga is known to modify the electronic structure of Pd, resulting in improved catalytic selectivity and stability (Kovnir et al., 2007).

For example, Pd-Ga alloys have demonstrated high efficiency and selectivity in the hydrogenation of acetylene to ethylene, a key process in the petrochemical industry. In this reaction, Pd alone tends to over-hydrogenate acetylene to ethane, which is undesirable. However, when alloyed with Ga, the over-hydrogenation tendency of Pd is suppressed, leading to higher ethylene selectivity (Kovnir et al., 2007; Studt et al., 2008). Furthermore, Pd-Ga alloys are also effective in the hydrogenation of CO₂ to methanol, a reaction of great interest for sustainable energy applications (Docherty & Copéret, 2021; Li et al., 2012). Moreover, Pd-Ga nanoparticles have been investigated for their use in alkane dehydrogenation reactions, where they exhibit enhanced stability compared to pure Pd catalysts. The alloy structure of Pd-Ga nanoparticles prevents catalyst deactivation due to coking (carbon deposition), which is a common issue in hydrocarbon processing (Sun & Li, 2022).

Consequently, to explore this approach combining spark ablation and metal-organic decomposition, we use trimethyl gallium (TMGa) {Ga (CH₃)₃}, a commonly used Ga precursor. TMGa is introduced into the aerosol stream where its methyl (CH₃) organic ligands undergo thermal decomposition, releasing Ga atoms. The Ga atoms then alloyed with metallic Pd nanoparticles, which are produced by spark ablation, forming Pd-Ga alloy nanoparticles. This reaction typically occurs in the gas phase before the particles are collected, enabling the in-flight synthesis of the alloy particles.

This approach builds upon a previous work by Snellman (2023) who demonstrated the production of sintered Au nanoparticles via spark ablation which were subsequently mixed with a stream of trimethyl indium (TMIn) in an optical chamber. The TMIn was decomposed through photolysis, resulting in the condensation of In atoms onto the Au nanoparticles. This process produced core-shell particles exhibiting diverse morphologies.

In the present study we present the production of Pd-Ga alloy nanoparticles, evaluating the influence of Ga precursor flows and sintering temperature on the morphology, composition and crystal structure of the compound particles. These findings highlight the importance of alloying in enhancing the functionality of Pd-based catalysts and the potential of spark ablation combined with metal-

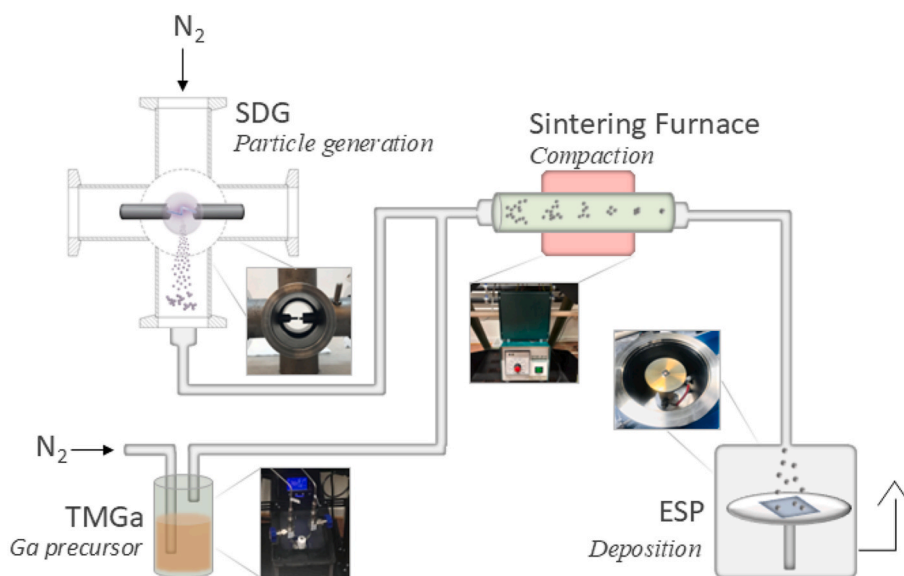


Fig. 1. Schematic overview of the generation of Pd-Ga alloy nanoparticles. Pd particles are generated in the SDG and TMGa is injected downstream the SDG, just before the sintering furnace in which the alloying process and particle compaction occur.

organic precursors for producing advanced nanomaterials.

It is worth noting that although the present experimental configuration was optimized for fundamental studies, spark ablation is a continuous process with potential for gram-scale nanoparticle generation (Feng et al., 2015; Stein & Kruis, 2018). Likewise, the use of TMGa as a precursor is widely established in research and commercial applications such as metal-organic vapour phase epitaxy (MOVPE), where precursor flows are readily adjustable. These aspects highlight the scalability potential of the method, which can be extended beyond the proof-of-concept experiments reported here.

2. Material and methods

2.1. Particle generation

Pd and Pd-Ga nanoparticles were produced using a setup as shown in Fig. 1. To generate Pd nanoparticles through spark ablation, two Pd rod electrodes of 3 mm diameter were loaded into a spark discharge generator (SDG) as described by Messing et al. (2010), keeping an electrode gap of approximately 2 mm, a discharge current of ca. 2.8 mA, and a discharge voltage of ca. 1.37 kV. A nitrogen (N_2) carrier gas was injected perpendicular to the rod-to-rod electrode configuration at a flow of 1.5 lpm carrying the as-generated Pd particles. A separate N_2 line at a flow of 1.5 lpm is used to uptake TMGa stored at -10°C in a gas bubbler and vapour pressure of 52.9 mbar, which is injected downstream of the SDG and upstream of the sintering furnace, where it mixes with the Pd particles. This saturated N_2 line with TMGa is set at flows of 1 sccm, 3 sccm, and 5 sccm, representing TMGa molar fractions of approximately 3.7×10^{-5} , 11.2×10^{-5} , and 18.6×10^{-5} , respectively. The sintering furnace which was set to either 750°C or 900°C , decomposes the TMGa, cracking the organic CH_3 ligands and freeing Ga atoms that, along with Pd nanoparticles, compact the as-produced agglomerates in a residence time of ca. 1.03 s forming Pd-Ga intermetallic compounds. Finally, since a sufficient fraction of the nanoparticles is charged due to the SDG process (Boeije et al., 2019), the resulting charged Pd-Ga nanoparticles are deposited on a substrate using an electrostatic precipitator (ESP) (Preger et al., 2020) at an approximately nominal particle surface density of 1000 particles $\cdot \mu\text{m}^{-2}$.

2.2. Characterization

The particle morphology was studied using a ZEISS Gemini 500 scanning electron microscopy (SEM) at an accelerating voltage of 15 kV and an In-lens detector.

Particle composition and crystal structure were analysed using transmission electron microscopy (TEM), high-resolution transmission electron microscopy (HRTEM), and selective area electron diffraction (SAED) patterns. For this purpose, Pd and Pd-Ga nanoparticles were deposited separately on lacey-carbon film-coated Cu TEM grids under identical spark ablation conditions (see section 2.1). To facilitate imaging of individual particles, the deposition time was adjusted to achieve a low particle surface density of approximately 50 particles $\cdot \mu\text{m}^{-2}$. The TEM grids were subsequently loaded into a single-tilt holder for imaging. The data presented here were acquired using a JEOL TEM 3000F equipped with a field emission gun and operated at 300 kV. Elemental mapping was performed using a high-angle annular dark-field (HAADF) detector coupled with an energy dispersive X-ray (EDX) spectrometer (Oxford Instruments) in scanning transmission electron microscopy (STEM) mode. The spectra were corrected for thickness and density and using the L-energy lines for both Ga and Pd, the particle composition was determined by the INCA software.

3. Results and discussion

SEM micrographs of Pd and Pd-Ga nanoparticles produced at 750°C and 900°C are shown in Fig. 2 (and Fig. S1 of the

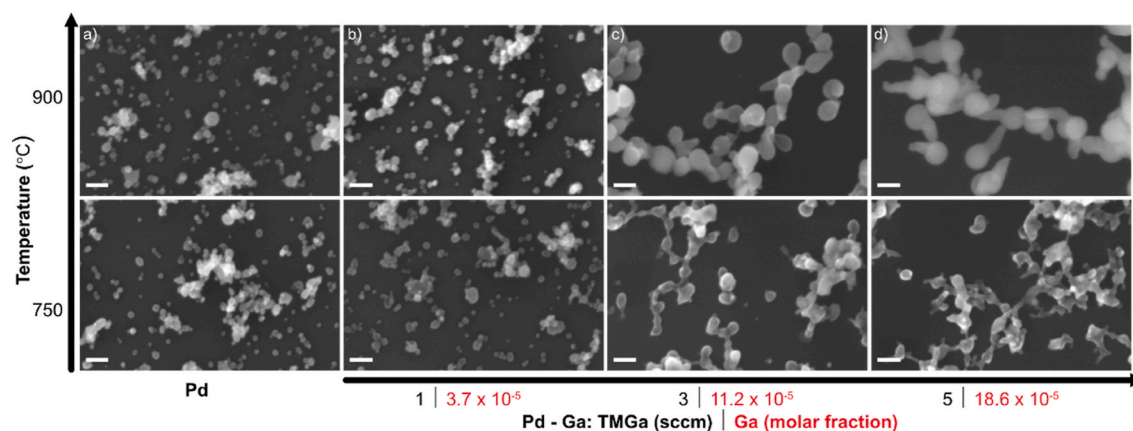


Fig. 2. SEM micrographs of nanoparticles produced at 750°C (bottom) and 900°C (top) of a) Pd, b) Pd-Ga at TMGa = 1 sccm, c) Pd-Ga at TMGa = 3 sccm, and d) Pd-Ga at TMGa = 5 sccm. Scale bar: 40 nm.

supplementary data), with varying TMGa concentrations through regulating the carrying flow from 1 sccm to 5 sccm. The morphological evolution of the nanoparticles correlates with the increasing TMGa flow. The alloying mechanism begins with Pd nanoparticles mixing with TMGa vapour prior to entering the sintering furnace. However, no significant alloying occurs at this stage since TMGa remains chemically intact and does not decompose at room temperature or in the mixing zone. Inside the sintering furnace, elevated temperatures induce the thermal decomposition of TMGa, releasing Ga atoms into the gas phase. These Ga atoms undergo heterogeneous nucleation on the surface of the preexisting spark-generated Pd nanoparticles rather than forming particles independently. Following nucleation, Ga atoms diffuse into the Pd lattice, leading to the formation and growth of Pd-Ga intermetallic phases. Thus, the overall alloying mechanism is governed by the sequence of TMGa decomposition, heterogeneous nucleation of Ga at Pd surfaces, atomic diffusion and intermetallic phase formation. Since spark ablation parameters (discharge current, discharge voltage, and electrode gap) remained constant for Pd nanoparticle generation, the observed changes in the alloyed particles are primarily driven by the TMGa flow rate and the sintering temperature.

At TMGa of 1 sccm, the size of the alloyed particles is comparable with pure Pd particles. At higher TMGa flows (3 sccm and 5 sccm), the particles show noticeable growth in size and increased aggregation, often forming chain-like structures. This trend is more pronounced at 900 °C, where Pd-Ga nanoparticles exhibit elongated or tail-like formations, especially at 5 sccm, likely resulting from a greater TMGa decomposition leading to Ga excess during particle growth and sintering. TMGa can thermally decompose under a nitrogen (N₂) atmosphere at temperatures above 550–660 °C to release Ga atoms (Larsen et al., 1990; Ye et al., 2020). Although the sintering temperature at 900 °C is well above this decomposition range, the efficiency of TMGa decomposition may increase significantly at higher temperatures, contributing to more pronounced Ga incorporation. This enhanced decomposition, combined with exposure at elevated temperatures, may promote the formation of Ga-rich phases.

The variation in Ga concentration can induce subtle changes in the structural and compositional nature of the nanoparticles, which are not easily captured by bulk or surface-sensitive techniques. Therefore, the morphology, composition, and crystal structure of Pd and Pd-Ga nanoparticles were further studied through TEM, HRTEM, STEM-EDX, and SAED. The as-produced Pd nanoparticles at 750 °C and 900 °C, shown in Fig. 3 present subtle differences where the latter appears to form more facets. At 900 °C, Pd atoms have higher kinetic energy, promoting faster diffusion across the nanoparticle surface. This facilitates the migration and reorganization of atoms into low-energy, well-defined crystallographic planes (facets), including {111} and {100}. In contrast, at 750 °C, Pd nanoparticles remain more spherical or irregular, probably due to slower atomic mobility and less reorganization.

As a separate remark, it is important to analyse the effect of the residence time during sintering on nanoparticle morphology. Generally, longer residence times lead to a densification of agglomerated particles (Seipenbusch et al., 2003), larger crystallite sizes, grain growth, and a possible formation of single-crystalline particles (Kocjan et al., 2017). The compaction process induces a particle rearrangement, with a subsequent reduction of particle mobility diameter (Seipenbusch et al., 2003), which may result in smoother and more regular surfaces. A comparison between Pd nanoparticles produced at 750 °C with a sintering residence time of 1.03 s (Fig. 3a and Fig. S1a of the supplementary data) and 5.46 s (Fig. S2 of the supplementary data) shows that the longer the sintering time, the more compact, spherical-like shape of Pd nanoparticles. Despite this, stacking faults and some facet formations are observed in both sets of nanoparticles, suggesting that while longer sintering may decrease surface defects, it does not eliminate them.

An elemental analysis from STEM-EDX of the Pd-Ga nanoparticles for a TMGa flow of 1 sccm produced at different sintering temperatures (750 °C and 900 °C) is shown in Fig. 4 and Table S1 in the supplementary data. For each sintering temperature, 65 nanoparticles of varying sizes were analysed. The data reveal a clear relationship between nanoparticle size, Ga and Pd content, suggesting the formation of various Pd-Ga phases depending on the particle diameter and sintering conditions.

At 750 °C, smaller nanoparticles (diameter ≤ 10 nm) exhibit low Ga content (6.0 at.%), indicating a strong Pd-dominated phase, due to kinetically limited Ga diffusion. As nanoparticle diameter increases (>10 nm), Ga content rises sharply to ~ 20 at.%, suggesting enhanced Ga mobility and potential formation of Pd-Ga intermetallic phases, such as Pd₅Ga₂, Pd₁₃Ga₅, Pd_{1-x}Ga_x and Pd_{2+x}Ga_{1-x} (Khalaff & Schubert, 1974; Wannek & Harbrecht, 2001).

At 900 °C, distinct trends emerge due to improved Ga diffusion, attributed to the high sintering temperature. All particle size categories—smallest (≤ 10 nm; 25.1 at.% Ga), mid-sized ($10 < D \leq 20$ nm; 25.0 at.% Ga) and larger particles (>20 nm; 23.5 at.% Ga)—converge near the overall average composition (75.5 at.% Pd, 24.5 at.% Ga). This uniformity suggests effective alloying even in small particles. Dominant phases likely include Pd₇Ga₃, Pd₅Ga₂, Pd₁₃Ga₅, Pd₂Ga, Pd_{2+x}Ga_{1-x}, and Pd_{1-x}Ga_x (Khalaff & Schubert, 1974; Wannek & Harbrecht, 2001).

The observed variations in standard deviation across temperatures and nanoparticle sizes highlight compositional heterogeneity,

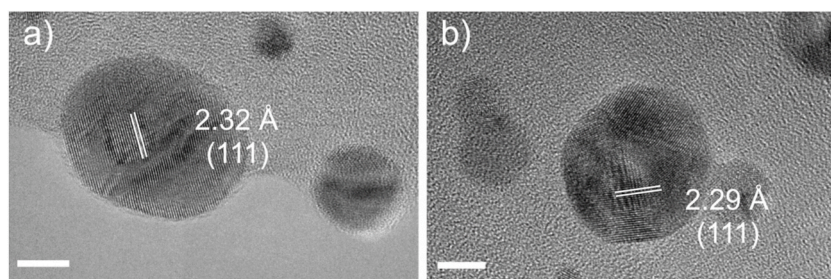


Fig. 3. HRTEM micrographs of Pd nanoparticles produced at a) 750 °C and b) 900 °C. Scale bar: 5 nm.

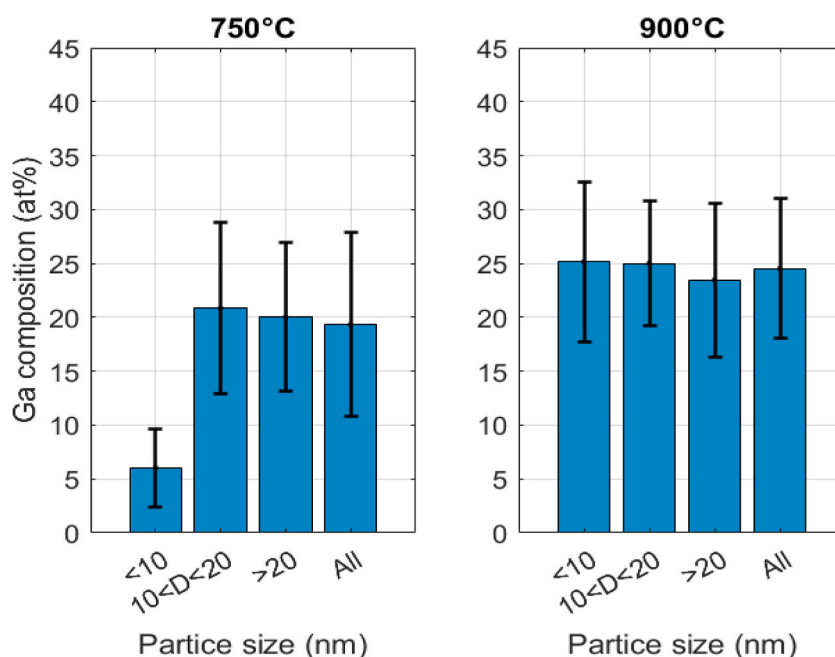


Fig. 4. Pd-Ga particle composition for a TMGa flow of 1 sccm at 750 °C and 900 °C.

suggesting variability in Ga incorporation and the coexistence of multiple Pd-Ga phases.

The Pd-Ga composition at 750 °C for Ga concentrations at 3 sccm and 5 sccm are shown in Fig. S3 in the supplementary data. The average Ga composition of 47.5 ± 6.4 at.% and 56.6 ± 9.4 at.% for TMGa at 3 sccm and 5 sccm, respectively, reveals a significant shift towards Ga-rich compositions.

Furthermore, as the nanoparticles produced at 900 °C exhibit significant morphological changes compared to those formed at 750 °C, a detailed analysis was carried out. HAADF-STEM and EDX mapping images in Fig. 5 illustrate the effect of increasing TMGa flow on the composition and morphology of Pd-Ga nanoparticles at 900 °C. At the lowest TMGa flow (1 sccm), the nanoparticles exhibit a uniform distribution of Pd and Ga, suggesting a stable alloying process. As the TMGa flow is increased to 3 sccm, a noticeable shift occurs, with Ga signals intensifying and Pd signals becoming more dispersed, indicating enhanced Ga incorporation and potential surface segregation, i.e., migration of Ga atoms towards the surface of the Pd-Ga alloy. By 5 sccm, the particles undergo significant morphological changes, elongating in a tail-like formation and showing a clear dominance of Ga, with Pd signals diminishing in relative intensity. A similar elongated particle morphology was observed by Magnusson (2001) when producing InP particles at increasing temperatures, where PH_3 cracking resulted in excess release of P atoms. This progression highlights the dynamic interplay between precursor flow and material composition, suggesting that lower TMGa flows promote more homogeneous Pd-Ga structures, whereas higher Ga precursor flows drive phase separation with Ga-rich domains (see Fig. S4 in the supplementary data). Additionally, Fig. 5b and c shows distinct areas of higher contrast (for heavier elements such as Pd) in the HAADF-STEM images, correlating with regions of increased Pd concentration. The EDX maps reveal that localized Pd signals are more intense near the nanoparticle core, while Ga dominates the outer regions, suggesting a core-shell-like structure (Fig. 5b). The contrast becomes more pronounced at 5 sccm, implying that the increased Ga precursor promotes surface accumulation of Ga while Pd segregates to an edge of the particle. When the concentration of Ga is sufficiently high, continued diffusion and supersaturation can drive surface segregation of Ga, resulting in the development of core-shell or phase-separated structures. These observations highlight the intricate balance between Pd and Ga during growth and the critical role of precursor flow rates in defining nanoparticle morphology and elemental distribution. It is worth noting that TEM-EDX measurements do not show carbon signals above background (see Fig. S5 in the supplementary data), confirming that methyl species from TMGa are fully decomposed, leaving no detectable incorporation of carbon in the Pd-Ga nanoparticles.

TEM and HRTEM images in Fig. 6 illustrate the structural evolution of Pd-Ga nanoparticles as a function of increasing TMGa flow, complementing the compositional analysis in Fig. 5. At 1 sccm (Fig. 6a), the overall morphology of the nanoparticles appears uniform, suggesting a stable alloying of Pd and Ga, and the particles exhibit well-defined crystalline structures with clear lattice fringes. The interplanar spacings (d-spacings) range between 2.22 Å and 2.25 Å. Although these d-spacings are close to pure Pd (d-spacing of 2.27 Å corresponding to (111) plane) (Meyer & Müller-Buschbaum, 1980), the elemental atomic composition and EDX mappings shown above indicate the presence of Pd-Ga phases. Therefore, these Pd-rich phases likely correspond to (210) plane of Pd_5Ga_2 (lattice parameters of $a = 5.48$ Å, $b = 4.08$ Å, and $c = 18.39$ Å) (Khalaff & Schubert, 1974), in good agreement with the compositional results shown in Fig. 4 and Table S1. The Pd_5Ga_2 phase has previously been studied as a catalyst in CO_2 selectivity in methanol steam reforming (Lorenz et al., 2009). Other Pd-Ga phases to explore in this regime due to comparable d-spacings include Pd_5Ga_3 , and Pd_3Ga which also show

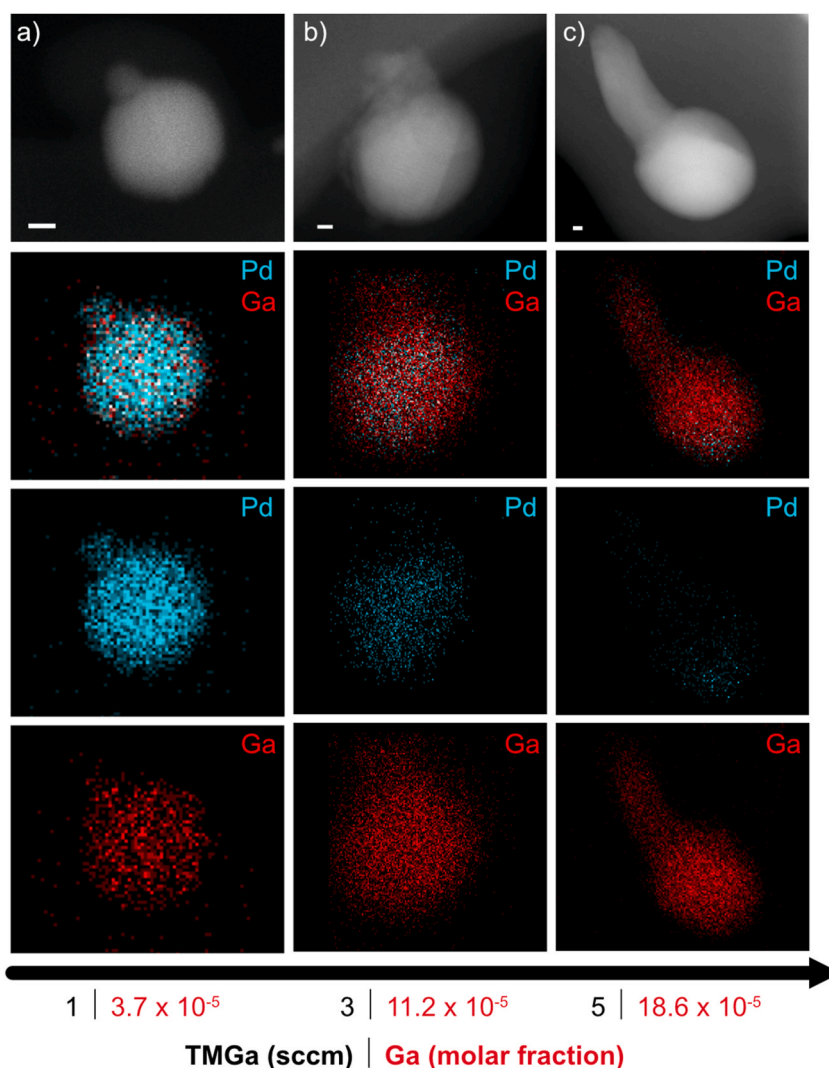


Fig. 5. HAADF-STEM and TEM-EDX mapping (convoluted Pd and Ga, Pd, and Ga signals, from top to bottom) of Pd-Ga nanoparticles at 900 °C at a) TMGa = 1 sccm, b) TMGa = 3 sccm, and c) TMGa = 5 sccm. Scale bar: 5 nm.

catalytic properties (Hou et al., 2018; Kaul & Ghosh, 2017).

As the TMGa flow is increased to 3 sccm (Fig. 6b), the formation of Pd₅Ga₂ persists, particularly near the edges of the round nanoparticles, with d-spacings of 2.22 Å. However, the tail-like region of the particle suggests the presence of Pd₂Ga (lattice parameters of a = 5.48 Å, b = 4.08 Å, and c = 7.79 Å) (Kovnir et al., 2008; Wannek & Harbrecht, 2001) with measured d-spacings between 2.47 Å and 2.58 Å in (112) plane and multiple grain orientations (Figs. 6b–2). This Pd₂Ga phase also presents catalytic properties with increasing selectivity in hydrogenation reactions (Armbrüster et al., 2010; Krajčí & Hafner, 2014).

At 5 sccm (Fig. 6c), the particles undergo significant morphological changes, elongating and forming chain-like structures shifting towards Ga-rich compositions. Nevertheless, sections of ordered structures appear with dominant PdGa phases and larger d-spacings of 4.88 Å and 4.94 Å along the (100) plane (Grin et al., 2016; Khalaff & Schubert, 1974; Kumar & Ghosh, 2016) which are known to exhibit enhanced catalytic properties in hydrogenation reactions (Armbrüster et al., 2010; Klanjšek et al., 2012; Kovnir et al., 2009). Like Fig. 6b, lattice fringes are primarily observed near the particle edges, suggesting that the areas further from the crystalline fringes appear amorphous due to the excess of Ga, which leads to phase separation and a loss of long-range order. EDX elemental analysis confirms that these areas possess 97.85 ± 2.15 at. % Ga, suggesting that Pd-Ga alloying occurs selectively, leaving Ga-dense zones structurally disordered, likely due to surface segregation of Ga as discussed above (Fig. 5).

To further confirm the phase evolution with TMGa flow, SAED patterns were acquired from clusters of particles, as shown in Fig. 7. At 1 sccm (Ga 3.7×10^{-5}), the reflections from the {210}, {400}, and {420} planes (d = 2.26, 1.37, and 1.14 Å) were indexed to the Pd₅Ga₂ phase. Increasing to 3 sccm (11.2×10^{-5}), two phases were identified: Pd₂Ga indexed to the {112} and {214} planes (d = 2.50 and 1.48 Å), and Pd₅Ga₂ indexed to {210} and {020} planes (d = 2.24 and 2.05 Å). At the highest Ga content of 5 sccm (Ga 18.6×10^{-5}), main dominant reflections from the {100}, {200}, and {300} planes (d = 4.92, 2.49, and 1.64 Å) indicated the formation of the

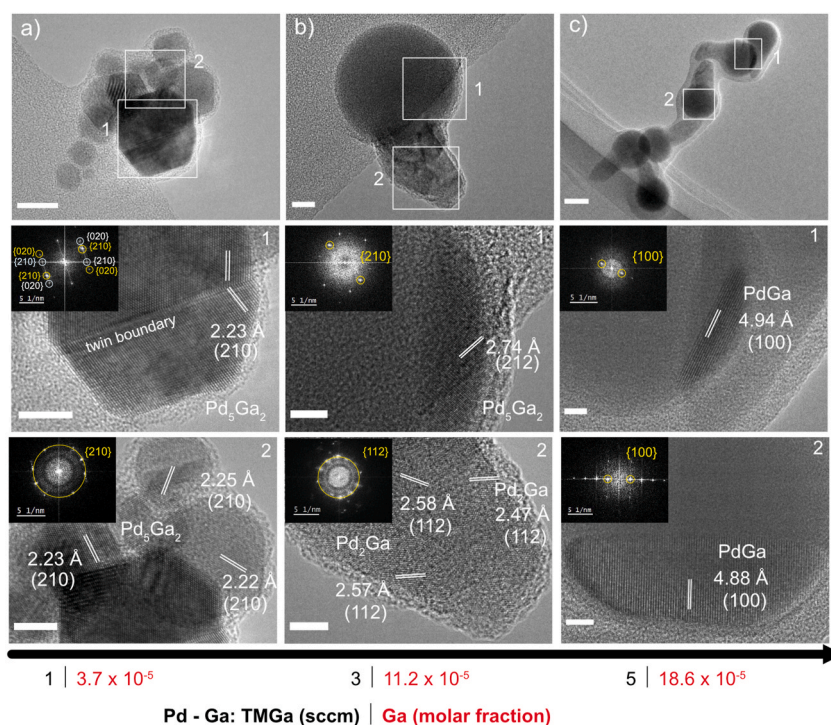


Fig. 6. TEM (1st row) and HRTEM (images 1 and 2) images with their corresponding FFTs (insets) of Pd-Ga nanoparticles produced at 900 °C at a) TMGa = 1 sccm, b) TMGa = 3 sccm, and c) TMGa = 5 sccm. Scale bar: 10 nm (a, b), 50 nm (c), and 5 nm (insets of a, b, and c).

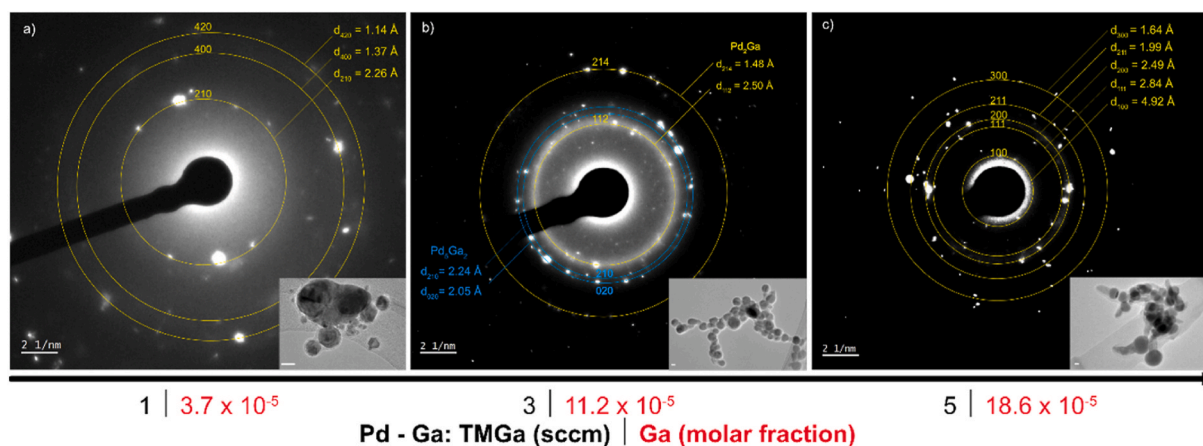


Fig. 7. SAED patterns of a cluster of particles (insets) of Pd-Ga nanoparticles produced at 900 °C at a) TMGa = 1 sccm, b) TMGa = 3 sccm, and c) TMGa = 5 sccm. Scale bar of insets: 20 nm.

PdGa intermetallic phase.

4. Conclusions

The combination of spark ablation and metal-organic precursor decomposition presents an effective and versatile method for producing Pd-Ga alloy nanoparticles with tunable composition and morphology. This synthesis method enables the formation of complex intermetallic phases, such as Pd_5Ga_2 , Pd_2Ga , and PdGa, by controlling precursor flow and sintering temperature. The results demonstrate that increasing TMGa flow drives the progression from homogeneous Pd-rich phases to a combination of particle elongation and aggregation with Ga-rich phases. High-temperature conditions (900 °C) enhance phase segregation and promote the formation of tail-like structures. The interplay between Pd and Ga at varying precursor concentrations not only influences nanoparticle morphology but also suggests pathways for tailoring Pd-Ga alloy nanoparticles with specific phase compositions. Future investigations

focused on fine-tuning the precursor supply and optimizing the sintering time could lead to better control of the resulting Pd-Ga compositions and access to more homogeneous Pd₂Ga, and PdGa phases. Moreover, this approach can be expanded to other metal-organic precursors, broadening the spectrum of alloy nanoparticles that can be generated and tailored for catalytic, electronic, and energy-related applications.

CRediT authorship contribution statement

Marie Bermeo: Writing – review & editing, Writing – original draft, Investigation, Formal analysis. **Markus Snellman:** Writing – review & editing, Methodology. **Linnéa Jönsson:** Writing – review & editing, Formal analysis, Data curation. **Thomas Krinke:** Writing – review & editing, Supervision. **Zhongshan Li:** Writing – review & editing, Supervision. **Knut Deppert:** Writing – review & editing, Supervision. **Maria E. Messing:** Writing – review & editing, Supervision.

Declaration of competing interest

The authors declare that they have no known competing financial interests or personal relationships that could have appeared to influence the work reported in this paper.

Acknowledgements

We acknowledge financial support from the Swedish Foundation for Strategic Research (Grant No. FFL18-0282), MyFab, and NanoLund. The project has received funding from the European Union's Horizon 2020 research and innovation programme under the Marie Skłodowska-Curie grant agreement No. 945378.

Appendix A. Supplementary data

Supplementary data to this article can be found online at <https://doi.org/10.1016/j.jaerosci.2025.106698>.

Data availability

Data will be made available on request.

References

- Armbrüster, M., Kovnir, K., Behrens, M., Teschner, D., Grin, Y., & Schlögl, R. (2010). Pd–Ga intermetallic compounds as highly selective semihydrogenation catalysts. *Journal of the American Chemical Society*, 132(42), 14745–14747. <https://doi.org/10.1021/ja106568t>, 2010/10/27.
- Boeije, M. F., Biskos, G., van der Maesen, B. E., Pfeiffer, T. V., van Vugt, A. W., Zijlstra, B., & Schmidt-Ott, A. (2019). Nanoparticle production by spark ablation: Principle, configurations, and basic steps toward application. In *Spark ablation* (pp. 49–108). Jenny Stanford Publishing.
- Deppert, K., Magnusson, M. H., Samuelson, L., Malm, J.-O., Svensson, C., & Bovin, J.-O. (1998). Size-selected nanocrystals of III–V semiconductor materials by the aerotaxy method. *Journal of Aerosol Science*, 29(5), 737–748, 1998/06/01/ <https://www.sciencedirect.com/science/article/pii/S0021850297100179>.
- Docherty, S. R., & Copéret, C. (2021). Deciphering metal–oxide and metal–metal interplay via surface organometallic chemistry: A case study with CO₂ hydrogenation to methanol. *Journal of the American Chemical Society*, 143(18), 6767–6780. <https://doi.org/10.1021/jacs.1c02555>, 2021/05/12.
- Efimov, A., Volkov, I., Varfolomeev, A., Vasiliev, A., & Ivanov, V. (2016). Tin oxide nanoparticles produced by spark ablation: Synthesis and gas sensing properties. *Oriental Journal of Chemistry*, 32, 2909–2913.
- Elmroth Nordlander, J., Bermeo, M., Ternero, P., Wahlqvist, D., Schmeida, T., Blomberg, S., Messing, M. E., Ek, M., & Hübner, J.-M. (2023). Mo₃Ni₂N nanoparticle generation by spark discharge. *Materials*, 16(3), 1113.
- Feng, J., Biskos, G., & Schmidt-Ott, A. (2015). Toward industrial scale synthesis of ultrapure singlet nanoparticles with controllable sizes in a continuous gas-phase process. *Scientific Reports*, 5(1), Article 15788.
- Franzén, S. M., Jönsson, L., Ternero, P., Kåredal, M., Eriksson, A. C., Blomberg, S., Hübner, J.-M., & Messing, M. E. (2023). Compositional tuning of gas-phase synthesized Pd–Cu nanoparticles. *Nanoscale Advances*, 5(22), 6069–6077.
- Grin, Y., Armbrüster, M., Baranov, A. I., Finzel, K., Kohout, M., Ormeci, A., Rosner, H., & Wagner, F. R. (2016). Atomic interactions in the intermetallic catalyst GaPd. *Molecular Physics*, 114(7–8), 1250–1259. <https://doi.org/10.1080/00268976.2015.1093664>, 2016/04/17.
- Gryaznov, V., Ermilova, M., Morozova, L., Orekhova, N., Polyakova, V., Roshan, N., Savitsky, E., & Parfenova, N. (1983). Palladium alloys as hydrogen permeable catalysts in hydrogenation and dehydrogenation reactions. *Journal of the Less Common Metals*, 89(2), 529–535.
- Hallberg, R. T., Ludvigsson, L., Preger, C., Meuller, B. O., Dick, K. A., & Messing, M. E. (2018). Hydrogen-assisted spark discharge generated metal nanoparticles to prevent oxide formation. *Aerosol Science and Technology*, 52(3), 347–358. <https://doi.org/10.1080/02786826.2017.1411580>, 2018/03/04.
- Hou, Z., Liu, Y., Deng, J., Lu, Y., Xie, S., Fang, X., & Dai, H. (2018). Highly Active and Stable Pd–GaOx/Al₂O₃ Catalysts Derived from Intermetallic Pd₅Ga₃ Nanocrystals for Methane Combustion. *ChemCatChem*, 10(24), 5637–5648. <https://doi.org/10.1002/cctc.201801684>.
- Jönsson, L., Snellman, M., Eriksson, A. C., Kåredal, M., Wallenberg, R., Blomberg, S., Kohut, A., Hartman, L., & Messing, M. E. (2024). The effect of electrode composition on bimetallic AgAu nanoparticles produced by spark ablation. *Journal of Aerosol Science*, 177, Article 106333, 2024/03/01/ <https://www.sciencedirect.com/science/article/pii/S0021850223001982>.
- Kaul, I., & Ghosh, P. (2017). First principles investigations of small bimetallic PdGa clusters as catalysts for hydrogen dissociation. *Chemical Physics*, 487, 87–96, 2017/04/20/ <https://www.sciencedirect.com/science/article/pii/S0301010416303810>.
- Khalaff, K., & Schubert, K. (1974). Kristallstruktur von Pd₅Ga₂. *Journal of the Less Common Metals*, 37(1), 129–140, 1974/07/01/ <https://www.sciencedirect.com/science/article/pii/0022508874900149>.

- Klanjšek, M., Gradišek, A., Kocjan, A., Bobnar, M., Jeglič, P., Wencka, M., Jagličić, Z., Popčević, P., Ivkov, J., Smontara, A., Gille, P., Armbrüster, M., Grin, Y., & Dolinšek, J. (2012). PdGa intermetallic hydrogenation catalyst: An NMR and physical property study. *Journal of Physics: Condensed Matter*, 24(8), Article 085703. <https://doi.org/10.1088/0953-8984/24/8/085703>, 2012/02/07.
- Kocjan, A., Logar, M., & Shen, Z. (2017). The agglomeration, coalescence and sliding of nanoparticles, leading to the rapid sintering of zirconia nanoceramics. *Scientific Reports*, 7(1), 2541. <https://doi.org/10.1038/s41598-017-02760-7>, 2017/05/31.
- Kovnir, K., Armbrüster, M., Teschner, D., Venkov, T. V., Jentoft, F. C., Knop-Gericke, A., Grin, Y., & Schlögl, R. (2007). A new approach to well-defined, stable and site-isolated catalysts. *Science and Technology of Advanced Materials*, 8(5), 420. <https://doi.org/10.1016/j.stam.2007.05.004>, 2007/07/31.
- Kovnir, K., Armbrüster, M., Teschner, D., Venkov, T. V., Szentmiklósi, L., Jentoft, F. C., Knop-Gericke, A., Grin, Y., & Schlögl, R. (2009). In situ surface characterization of the intermetallic compound PdGa – A highly selective hydrogenation catalyst. *Surface Science*, 603(10), 1784–1792. <https://doi.org/10.1016/j.susc.2008.09.058>, 2009/06/01/.
- Kovnir, K., Schmidt, M., Waurisch, C., Armbrüster, M., Prots, Y., & Grin, Y. (2008). Refinement of the crystal structure of dipalladium gallium, Pd₂Ga. *Zeitschrift für Kristallographie - New Crystal Structures*, 223(1), 7–8. <https://doi.org/10.1524/ncrs.2008.0004>
- Krajčí, M., & Hafner, J. (2014). Semihydrogenation of acetylene on the (010) surface of GaPd₂: Ga enrichment improves selectivity. *Journal of Physical Chemistry C*, 118(23), 12285–12301. <https://doi.org/10.1021/jp5025075>, 2014/06/12.
- Kumar, N., & Ghosh, P. (2016). Structure and stability of clean and adsorbate covered intermetallic PdGa surfaces: A first principles study. *Surface Science*, 644, 69–79, 2016/02/01/ <https://www.sciencedirect.com/science/article/pii/S0039602815002757>.
- Larsen, C. A., Buchan, N. I., Li, S. H., & Stringfellow, G. B. (1990). 1990/04/02/. Decomposition mechanisms of trimethylgallium. *Journal of Crystal Growth*, 102(1), 103–116. <https://www.sciencedirect.com/science/article/pii/002202489090891N>.
- Li, L., Zhang, B., Kunkes, E., Föttinger, K., Armbrüster, M., Su, D. S., Wei, W., Schlögl, R., & Behrens, M. (2012). Ga-Pd/Ga₂O₃ catalysts: The role of gallia polymorphs, intermetallic compounds, and pretreatment conditions on selectivity and stability in different reactions. *ChemCatChem*, 4(11), 1764–1775. <https://chemistry-europe.onlinelibrary.wiley.com/doi/abs/10.1002/cctc.201200268>.
- Lorenz, H., Penner, S., Jochum, W., Rameshan, C., & Klötzer, B. (2009). Pd/Ga₂O₃ methanol steam reforming catalysts: Part II. Catalytic selectivity. *Applied Catalysis A: General*, 358(2), 203–210, 2009/05/01/ <https://www.sciencedirect.com/science/article/pii/S0926860X09001331>.
- Magnusson, M. (2001). *Metal and semiconductor nanocrystals for quantum devices*. Lund University.
- Messing, M. E., Westerström, R., Meuller, B. O., Blomberg, S., Gustafson, J., Andersen, J. N., Lundgren, E., van Rijn, R., Balmes, O., Bluhm, H., & Deppert, K. (2010). Generation of Pd model catalyst nanoparticles by spark discharge. *Journal of Physical Chemistry C*, 114(20), 9257–9263. <https://doi.org/10.1021/jp101390a>, 2010/05/27.
- Meuller, B. O., Messing, M. E., Engberg, D. L. J., Jansson, A. M., Johansson, L. I. M., Norlén, S. M., Tureson, N., & Deppert, K. (2012). Review of spark discharge generators for production of nanoparticle aerosols. *Aerosol Science and Technology*, 46(11), 1256–1270. <https://doi.org/10.1080/02786826.2012.705448>, 2012/11/01.
- Meyer, H. J., & Müller-Buschbaum, H. K. (1980). Eine neue durch oxidspure stabilisierte form des palladiums. *Journal of the Less Common Metals*, 76(1), 293–298, 1980/12/01/ <https://www.sciencedirect.com/science/article/pii/0022508880900326>.
- Muntean, A., Wagner, M., Meyer, J., & Seipenbusch, M. (2016). Generation of copper, nickel, and CuNi alloy nanoparticles by spark discharge. *Journal of Nanoparticle Research*, 18, 1–9.
- Preger, C., Overgaard, N. C., Messing, M. E., & Magnusson, M. H. (2020). Predicting the deposition spot radius and the nanoparticle concentration distribution in an electrostatic precipitator. *Aerosol Science and Technology*, 54(6), 718–728.
- Seipenbusch, M., Weber, A., Schiel, A., & Kasper, G. (2003). Influence of the gas atmosphere on restructuring and sintering kinetics of nickel and platinum aerosol nanoparticle agglomerates. *Journal of Aerosol Science*, 34(12), 1699–1709.
- Snellman, M. (2023). *Aerosol synthesis and characterization of heterogeneous bimetallic nanoparticles*.
- Snellman, M., Eom, N., Ek, M., Messing, M. E., & Deppert, K. (2021). Continuous gas-phase synthesis of core-shell nanoparticles via surface segregation. *Nanoscale Advances*, 3(11), 3041–3052.
- Stein, M., & Kruijs, F. E. (2018). Scaling-up metal nanoparticle production by transferred arc discharge. *Advanced Powder Technology*, 29(12), 3138–3144. <https://doi.org/10.1016/j.apt.2018.08.016>, 2018/12/01/.
- Studt, F., Abild-Pedersen, F., Bligaard, T., Sørensen, R. Z., Christensen, C. H., & Nørskov, J. K. (2008). On the role of surface modifications of palladium catalysts in the selective hydrogenation of acetylene. *Angewandte Chemie International Edition*, 47(48), 9299–9302. <https://onlinelibrary.wiley.com/doi/abs/10.1002/anie.200802844>.
- Sun, X., & Li, H. (2022). Recent progress of Ga-based liquid metals in catalysis. *RSC Advances*, 12(38), 24946–24957.
- Ternero, P., Preger, C., Eriksson, A. C., Rissler, J., Hübner, J.-M., & Messing, M. E. (2024). In-Flight tuning of Au-Sn nanoparticle properties. *Langmuir*, 40(31), 16393–16399. <https://doi.org/10.1021/acs.langmuir.4c01656>, 2024/08/06.
- Wannek, C., & Harbrecht, B. (2001). Phase equilibria in the palladium-rich part of the gallium–palladium system. The crystal structures of Ga₃Pd₇ and Ga₁–xPd_{2+x}. *Journal of Alloys and Compounds*, 316(1–2), 99–106.
- Ye, Z., Nitta, S., Honda, Y., Pristovsek, M., & Amano, H. (2020). Analysis of trimethylgallium decomposition by high-resolution mass spectrometry. *Japanese Journal of Applied Physics*, 59(2), Article 025511. <https://doi.org/10.35848/1347-4065/ab6fb0>, 2020/02/01.